N-doped sponge-like biochar: A promising CO2 sorbent for CO/CH and CO2/N gas separation

Chemical Engineering Journal 470 (2023) 144005

Contents lists available at ScienceDirect

Chemical Engineering Journal

journal homepage: www.elsevier.com/locate/cej

N-doped sponge-like biochar: A promising CO_2 sorbent for CO_2/CH_4 and CO_2/N_2 gas separation

Mirtha A.O. Lourenço [a,b,*], Tânia Frade [c], Marta Bordonhos [a,c], Micaela Castellino [d], Moisés L. Pinto [c], Sergio Bocchini [b,d]

[a] CICECO – Instituto de Materiais de Aveiro, Departamento de Química, Universidade de Aveiro, Campus Universitário de Santiago, 3810-193 Aveiro, Portugal
[b] Istituto Italiano di Tecnologia – IIT, Center for Sustainable Future Technologies (CSFT), Via Livorno 60, 10144 Torino, Italy
[c] CERENA, Departamento de Engenharia Química, Instituto Superior Técnico, Universidade de Lisboa, 1049-001 Lisboa, Portugal
[d] Department of Applied Science and Technology (DISAT), Politecnico di Torino, Corso Duca degli Abruzzi 24, 10129 Torino, Italy

ARTICLE INFO

Keywords:
Biochar
Pyrolyzed chitosan
CO_2 capture
Gas adsorption-separation

ABSTRACT

Sponge-like biochar sorbents were prepared from the dissolution of chitosan followed by freeze-drying methodology and pyrolysis at three different temperatures (400, 600, and 800 °C) to produce sustainable N-enriched carbon materials with enhanced CO_2 uptake from CO_2/CH_4 and CO_2/N_2 gas mixtures. The pyrolysis process was reproduced by *operando* TGA-IR to study the gas evolved from the pyrolysis process. It was found that the pyrolysis temperature highly influences the textural properties of the chitosan sponge-like biochar materials, impacting mainly the amount and type of the N-species on the sample but also at the microporosity. XPS revealed the transformation of the amino groups from chitosan into pyridinic-N, pyrrolic-N, graphitic center-N, and graphitic valley-N or pyridine-N oxide species during the pyrolysis process. Increasing the pyrolysis temperature enhanced the quantity of the latter two N-type species. All sponge-like biochars adsorbed higher amounts of CO_2 compared with CH_4 and N_2 gases, with maximum CO_2 uptake (~1.6 mmol·g^{-1}) at 100 kPa and 25 °C for the sample pyrolyzed at 600 °C (named CTO_P600). Biochar produced at 800 °C showed no longer adsorption capacity for CH_4 and N_2, having the highest selectivity value for CO_2/N_2 separation under continuous flux conditions among all prepared biochar sorbents. Isobaric CO_2 adsorption measurements on the CTO_P600 sorbent revealed that physisorption phenomena predominantly governed the CO_2 adsorption process, which was confirmed by its consistent adsorption capacity after 10 consecutive adsorption–desorption cycles. Moreover, the biochar exhibited tolerance to water vapor adsorption, indicating its suitability to work under moisture-rich conditions.

1. Introduction

Carbon dioxide (CO_2) is one of the major greenhouse gases (GHG) that contributes to global warming and is significantly produced from anthropogenic sources [1-4]. To reduce GHG emissions, CO_2 capture, usage, and storage (CCUS) technologies have been pursued [2,4,5]. Currently, the most common commercial technology for CO_2 uptake is based on the absorption process by employing liquid amines like monoethanolamine (MEA) and diethanolamine (DEA) [1]. However, this method has significant negative human and environmental drawbacks, requiring a large amount of energy [1] and making amine scrubbing impractical for some CO_2 uptake applications, like biogas upgrading or flue gas cleaning from the cement industry [1,2,6]. Therefore, it is essential to develop cost-effective sorbents from sustainable sources like biomass that can efficiently adsorb CO_2 and be used in large-scale post-combustion technologies or biogas upgrading. Among all sorbents, carbon materials are physical adsorbents with a high potential for CO_2 capture. They are less sensitive to moisture, have high adsorption capacity at ambient pressure, are more stable, easily regenerated, and require less power than conventional chemical processes [1,5,7]. However, most of these CO_2 adsorbents show low selectivity for CO_2/N_2 and CO_2/CH_4 separation processes or are relatively high priced.

Biochar, a carbon-based solid, can be obtained by pyrolysis of biomass. The unique features of biochar (namely thermal and chemical

* Corresponding author at: CICECO – Instituto de Materiais de Aveiro, Departamento de Química, Universidade de Aveiro, Campus Universitário de Santiago, 3810-193 Aveiro, Portugal
E-mail address: mirtha@ua.pt (M.A.O. Lourenço).

https://doi.org/10.1016/j.cej.2023.144005
Received 14 February 2023; Received in revised form 30 May 2023; Accepted 6 June 2023
Available online 8 June 2023

stabilities) combined with a wide range of chemical compositions and surface properties (that can be obtained depending on the biomass source and synthesis conditions) are advantageous for CO_2 adsorption [8,9]. Still, there is a scarcity of studies using novel and optimized methods to enhance the biochar adsorption properties [10,11] and in understanding the solid–gas interfaces at the material surface as it occurs with porous silicas [12-16].

Perilla biochar [11], among other tested biochars (derived from soybean stover, Korean oak, and Japanese oak), showed the highest adsorption capacity and removal rate for H_2S and CO_2 gases from biogas due to the higher N amount, surface area, and mesoporosity. Yet, perilla leaf is used in Asian cuisine and Chinese medicine, and no selectivity and reusability were studied, essential for industrial application. Wang *et al.* [17] prepared algae-derived nitrogen-containing porous carbons for CO_2/CH_4 and CO_2/N_2 adsorption-separation. The materials showed good CO_2 adsorption capacity (maximum 3.9 mmol·g^{-1}) and CO_2/CH_4 and CO_2/N_2 selectivities at 100 kPa (with maximum values of 49 and 16.9, respectively). However, the synthesis process uses pulverized KOH before pyrolysis, and the study of the adsorption measurements considering pressures higher than 100 kPa and under humid conditions is missing. Duràn *et al.* [18] synthesized a lignocellulosic-based activated carbon for biogas upgrading. The authors carried out binary CO_2/CH_4 breakthrough experiments at 30 °C under different gas compositions and adsorption pressures in a fixed-bed lab set-up to determine the competitive adsorption behavior of the activated carbon sample under dry and humid conditions. This material adsorbed 2 mmol·g^{-1} of CO_2 at 120 kPa and 30 °C in a binary CO_2/CH_4 (50/50 vol.%) mixture, but the selectivity for CO_2 over CH_4 was only 5.23 under dry conditions. Under humid conditions, the CO_2 adsorption capacity and the CO_2/CH_4 selectivity decreased to 1.39 and 3.36 mmol·g^{-1}, respectively. Lourenço *et al.* [10] prepared and tested biochar derived from chitosan with different surface areas, pore sizes, and N content and tested these sorbents on CO_2/CH_4 adsorption-separation. The authors observed that the drying method (supercritical CO_2, vacuum, or muffle under 40 °C) influenced the biochar microstructure and chemistry of the final material. Pyrolyzed chitosan spheres previously dried with supercritical CO_2 had the highest CO_2 adsorption capacity, selectivity, and easy regeneration compared with the samples dried using the other methods [10]. Nevertheless, the synthesis to prepare the chitosan alcohol beads is complicated and very time-consuming, and the adsorption kinetics of the obtained material is very slow, being relevant to enhance the method. Also, it is important to study the competitive adsorption of CO_2/N_2 and CO_2/H_2O gas mixtures and cyclic stability.

Here, we describe the preparation of sponge-like chitosan biochar sorbents for gas separation processes. Three biochar samples are prepared using a simple method by freeze-drying a chitosan solution followed by pyrolysis at different temperatures (400, 600, and 800 °C). Thermogravimetric analysis coupled with infrared spectroscopy (TGA-IR) is used to study the gases that evolve during the pyrolysis process at different temperatures, while X-ray photoelectron spectroscopy (XPS) provides information about the functional groups of the produced samples. Biochar materials are tested by measuring the pure CO_2, CH_4, and N_2 adsorption isotherms (at pressures up to 1000 kPa and 25 °C) to assess their potential for CO_2 separation from mixtures with N_2 and CH_4. The results are correlated with the materials' textural properties (specific surface area, pore volume, N content, and chemical species) to understand their relationship with CO_2 adsorption and CO_2/CH_4 and CO_2/N_2 separation ability. The ability to capture CO_2 in a 20% mixture of CO_2/N_2 in a continuous flux process is determined for all biochar materials. Finally, the best-performing sample is tested for pure CO_2 adsorption up to the atmospheric pressure and at different temperatures (30 – 80 °C), on water adsorption–desorption isotherm, on CO_2 adsorption isotherms under varied moisture conditions, and on 10 CO_2 adsorption–desorption cycles to study its sensitivity to temperature, humidity, and reusability, which are relevant aspects for industrial gas separation operation conditions.

2. Experimental details

2.1. Chemicals

Chitosan (medium molecular weight, 190,000 – 310000 Da, CAS number 9012–76-4) and acetic acid (glacial, 100%) were purchased from Sigma-Aldrich and used as received.

2.2. Pyrolyzed chitosan

Chitosan (CTO) based biochar was synthesized using a similar method described by Lourenço *et al.* [19]. Typically, chitosan (1.5 wt.%) was added to an acetic acid aqueous solution (268 mL, 0.1 M) and stirred overnight at room temperature. The chitosan solution was filtered-off, frozen overnight, and freeze-dried for 72 h. The obtained sponge-like chitosan aerogel was pyrolyzed under N_2 flux using the following heating procedure: i) 5 °C·min^{-1}, 200 °C, 2 h and ii) 5 °C·min^{-1}, final temperature, 2 h, where the final temperature can be 400, 600 or 800 °C. Scheme S1, in the Supplementary Material (SM), shows a schematic representation of the synthesis of the biochar samples. The obtained pyrolyzed chitosan-based material was named CTO_P*x*, where *x* can be 400, 600, and 800, and the weight loss after the pyrolysis process is 68.26, 74.12 and 74.45 %, respectively.

2.3. Characterization

The materials prepared in this study were characterized by field emission scanning electronic microscopy (FESEM), 77 K (−196 °C) nitrogen adsorption–desorption isotherms, thermogravimetric analysis (TGA), *operando* TGA – infrared (IR) spectroscopy (TGA-IR), elemental analysis (EA), and X-ray photoelectron spectroscopy (XPS). Pure CO_2, N_2, and CH_4 adsorption measurements on the biochar materials were performed using a lab-made stainless steel volumetric apparatus at 0, 25, and 35 °C up to 1000 kPa. Adsorption measurements of 20 vol.% of CO_2 in a mixture of N_2/CO_2 were made in an operando TGA-IR apparatus at 35 °C and atmospheric pressure. A Dynamic Vapor Sorption (DVS) instrument was used to acquire pure CO_2 adsorption isotherm up to 89 kPa at 30 °C, pure CO_2 adsorption isobar up to 80 °C and 20 kPa, water vapor adsorption–desorption and CO_2 adsorption–desorption isotherms under different moisture conditions at 30 °C, and reusability tests for the best-performing sample. The equipment and experimental parameters used are described in the SM.

3. Results and discussion

3.1. Characterization of materials

The assessment of the gases evolved from the biochar synthesis at various temperatures was performed using the *operando* TGA-IR technique (Fig. 1 and Figures S1 and S2, SM). The same initial sponge-like chitosan batch was used for the pyrolysis at 400, 600, and 800 °C under N_2 flux to prevent any variability in the synthetic conditions arising from chitosan aerogel production. Fig. 1 reports the thermal treatment of the chitosan into TGA at 200 °C for 100 min and the behavior at further heating to 800 °C; the other treatment up to 400 °C and 600 °C are reported in the SM.

For all pyrolyzed processes, the first heating step, up to 200 °C, promotes a weight loss of 20 – 22% which is mainly due to the evaporation of acetic acid that remains from the chitosan dissolution process (*cf.* IR information in Fig. 1b, and Figures S1 and S2). This behavior contrasts with the literature, where this weight loss corresponds to the evaporation of physically adsorbed and strongly hydrogen-bonded water on the commercial powdered chitosan [20], which was studied as received. Thus, the differences observed between both studies are related to the sample preparation differences. During the thermal treatment at 200 °C, the material continues releasing acetic acid. CO_2,

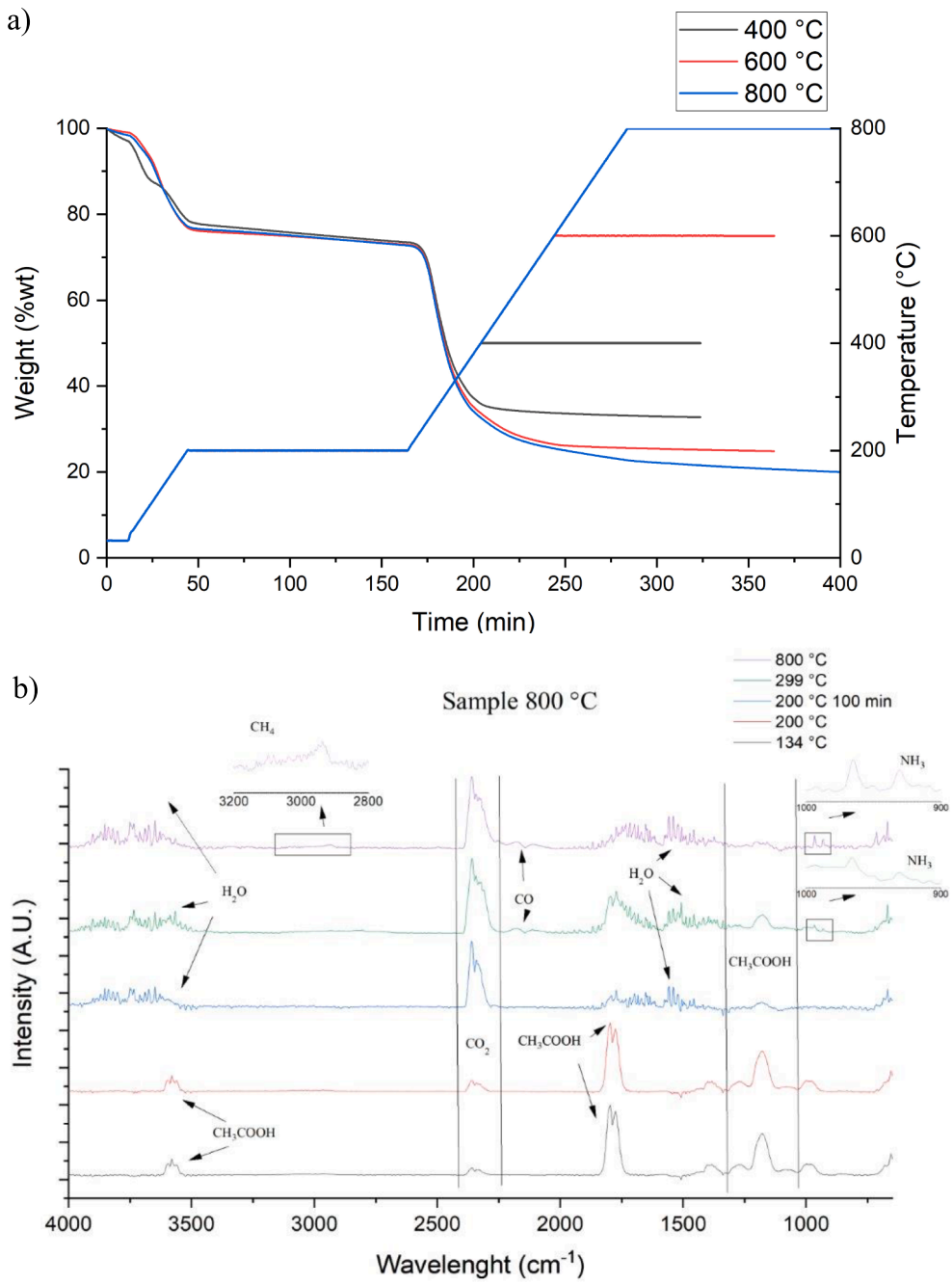

Fig. 1. a) schematic representation of the pyrolysis process at different temperatures and b) IR spectra of the developed gases at 134, 200, 200 (at 100 min), 299, and 800 °C under N_2 flow, obtained during the pyrolysis process to obtain CTO_P800 sample.

CO, NH_3, and H_2O start to develop in the pyrolysis process of the chitosan sponge-like material probably induced by the acidic conditions. Hetero-atomic rings containing the nitrogen not released at this stage during the random breaking of C – O – C skeletal bonds start to form, as reported in previous studies [21,22]. Finally, the last weight loss of *ca.* 40 – 50 wt.% (depending on the final pyrolysis temperature) occurs mainly between 250 and 450 °C and continues to produce the following species: CO_2, CO, NH_3, H_2O, CH_3COOH, and CH_4. CH_4 probably derives mainly from the partial thermal degradation of residue acetic acid to CH_4 and CO_2 but also from the consequent formation of graphite-like structures via a dehydrogenation mechanism [20]. The other gases appear due to the thermal destruction/transformation of glucosamine and pyranose rings and the decomposition of residual carbon [20,23]. The remaining mass after pyrolysis is attributed to the resulting biochar at different temperatures. The weight loss observed in the operando TGA-IR measurements of the pyrolysis process matches the results obtained through experimental analysis in a conventional oven: 68.26, 74.12, and 74.45 wt·% for CTO_P400, CTO_P600, and CTO_P800, respectively.

Table S1 (SM) shows the N content obtained in the chitosan materials pyrolyzed at different temperatures determined by elemental analysis. All samples retain a substantial amount of nitrogen, indicating that the N groups of chitosan are present in the structure of the pyrolyzed chitosan samples. The sponge-like biochar material with the highest N content is CTO_P400 (9.9 wt.%), and this value decreases with increasing pyrolysis temperature, reaching 6.4 wt.% for the CTO_P800 sample. These results

agree with *operando* TGA-IR measurements, which showed that NH_3 (evolved from the degradation of chitosan) continues to be released up to 800 °C (Fig. 1).

The chemical features of the different biochar materials prepared in this study, as well as the pristine chitosan powder precursor and sponge-like chitosan material, were assessed by XPS. The analysis of XPS allowed us to determine firstly the relative atomic concentration (at.%) of each element present on the samples' surfaces (as reported in Table 1), calculated from high-resolution (HR) spectra, to be much more precise in the peak area evaluation procedure. In Figure S3, survey spectra showed a clear trend in the oxygen peak evolution, having the highest intensity in the chitosan powder precursor and the lowest for the CTO_P800 sample. The N content trend in the pyrolyzed samples is distinct since sample CTO_P400 has the highest concentration (8.9 at.%), while the sponge-like chitosan aerogel has the lowest (3.4 at.%). The increase in the pyrolysis temperature promotes a reduction in the N content, which is in accordance with TGA and EA data. C1s core level peak has been first analyzed to establish the relative amount of graphitic species, together with bonds related to oxygen and/or nitrogen atoms. To perform the deconvolution procedure of the C1s peak (Fig. 2a), we have chosen as references some detailed works related to chitosan studies [24,25]. Apart from the well-known chemical shifts due to C − C/C-H (at 284.5 eV), there are chemical shifts due to C interactions with O and/or N at 286.2 eV (C − O/N), 287.5 eV (O − C − O/C = O), 288.5 eV (O − C = O) and the shake-up satellite due to π – π* transition at binding energy (BE) > 291 eV, for carbon in aromatic compounds, coming from the ring excited by the exiting photoelectrons. The π bond is a characteristic feature of the sp^2 hybridization of carbon. The deconvolution procedures and chemical species relative percentages are displayed in Fig. 2a and Table 1.

There is a trend in reducing the components related to C − O/N bonds especially passing from chitosan precursor and polymer to pyrolyzed samples, which agrees with the reduction of O and N peaks intensity, as reported in the survey spectra (Figure S3) and Table 1. Moreover, the increase in the pyrolysis temperature (T) coincides with a reduction of the full width at half maximum (FWHM) of the C-C/H component (from 1.56 eV for CTO_P400 to 1.20 eV for CTO_P800), which is a clear hint of a more ordered structure, due to the graphitization process induced. Also, the π – π* component (peak V) increases according to T, passing from 1.5 % (sample CTO_P400) to 4.8 % for the sample treated at 800 °C, representing a further indication of the graphitization process. The non-monotonic trends observed in this study (in Table 1 – *e.g.*, C − C/C − H) are not uncommon in the literature on biochar thermal treatments [26]. For example, grass-derived and wood-derived biochar [27] exhibit changes in electronic exchange capacity as the temperature increases, with an oscillating behavior in grass-derived samples (with a maximum at 400 °C) and a less oscillating trend with a peak shift (but with a maximum shift at 500 °C) in wood-derived samples. These peaks were associated with an abundance of quinoid group content measured by Near-edge X-ray absorption fine structure (NEXAFS).

Table 1
XPS relative atomic concentration and C1s and N1s core level assignments evaluated from deconvolution procedures (reported in Figures 2 and S3, respectively).

	Chitosan powder	Chitosan aerogel	CTO_P400	CTO_P600	CTO_P800
Relative atomic concentration (at.%)					
C1s	68.0	81.4	77.8	85.8	89.3
O1s	27.0	15.2	13.3	7.7	5.6
N1s	5.0	3.4	8.9	6.5	5.1
Carbon species (%)					
C − C/C − H	56.2	69.4	63.2	67.9	63.2
C − O/N	34.0	18.6	23.9	18.1	16.6
O − C − O/C = O	7.0	7.4	7.3	7.0	10.4
O − C = O/COOH	2.8	4.6	4.1	4.0	5.0
π − π*	/	/	1.5	3.0	4.8
Nitrogen species (%)					
Pyridinic-N	/	/	47.9	43.6	35.6
Amino-group	100	100	18.0	11.7	7.9
Pyrrolic-N	/	/	24.4	27.5	16.9
Graphitic center-N	/	/	5.1	8.2	21.8
Graphitic valley-N or pyridine-N oxide	/	/	4.6	9.0	17.8

From the N1s core level peaks, the different nitrogen species present in each sample were evaluated, as reported in Table 1 and Fig. 2b. Chitosan powder precursor and sponge-like aerogel showed only one type of nitrogen species, the amino group (named peak II), as expected from their chemical structure. The thermally treated samples have shown four more components assigned to: pyridinic-N (peak I), Pyrrolic-N (peak III), graphitic center-N (peak IV), and graphitic valley-N or pyridine-N oxide (peak V) [28-30]. There are three noticeable trends in the pyrolyzed biochar samples: following the temperature increase, there is a decrease in peak I intensity and an increase in peak IV and V. This is visible in Fig. 2b, in which the N1s peaks of the chitosan precursor and aerogel materials show only one component (amino group), while by increasing temperature there is a sort of splitting in the peak envelope, due to the increase of peak IV and V, due to graphitic components. In the case of the CTO biochar thermally treated at 800 °C for 2 h, the presence of pyridone-N species is more likely to occur than pyrrole-like N species, as the former is more stable at elevated temperatures [31]. This uncertainty to truly distinguish pyridone and pyrrole-like N species is due to peaks overlapping.

To ensure the effective degassing of the biochar samples without compromising their structural integrity, the thermal stability of the biochar samples under N_2 flux was investigated by TGA. Figure S4 shows that the thermal stability of the biochar samples under N_2 flow increases by rising the pyrolysis temperature, with CTO_P400 being the sample with the lowest thermal stability (up to 180 °C). Up to this temperature, just the adsorbed water and gases are released by all the biochar materials. As expected, thermal stability increases with the increase of the final pyrolysis temperature, with the CTO_P800 having the highest thermal stability, up to 750 °C.

The physical and textural properties of the biochar sorbents were studied by 77 K (−196 °C) N_2 adsorption–desorption isotherms and FESEM. In Figure S5, it is possible to observe that the chitosan samples pyrolyzed at different temperatures display a Type II curve (IUPAC classification) [32], usually observed for nonporous or macroporous materials. The specific surface area (S_{BET}) determined by applying the theory proposed by Brunauer-Emmett-Teller (BET), and pore volume of the pyrolyzed chitosan-based biochar materials are low, with values ranging between 11 and 18 $m^2 \cdot g^{-1}$ and 0.013 and 0.030 $cm^3 \cdot g^{-1}$), respectively, as expected. Biochar samples typically have low N_2 adsorption capacity at cryogenic temperatures, as the porous structure of these materials is almost entirely composed of ultra-micropores [33]. At 77 K (−196 °C), the diffusion rate of the N_2 molecules into ultra-micropores is extremely slow [34], leading to very low values of S_{BET} for some biochars, which is the case of the present studied materials. According to P. Maziarka *et al.* [35], N_2 adsorption–desorption isotherms can be unreliable determining conventional surface area and pore size distribution (PSD) curves of biochars. To address this, the authors proposed that a separate CO_2 characterization should be conducted in conjunction with N_2 sorption isotherm to obtain information about narrow micropores, as demonstrated by A. Diéguez-Alonso *et al.* [36]. Additionally, an adjusted density functional theory (DFT) calculation can be applied to more accurately assess the microporosity of

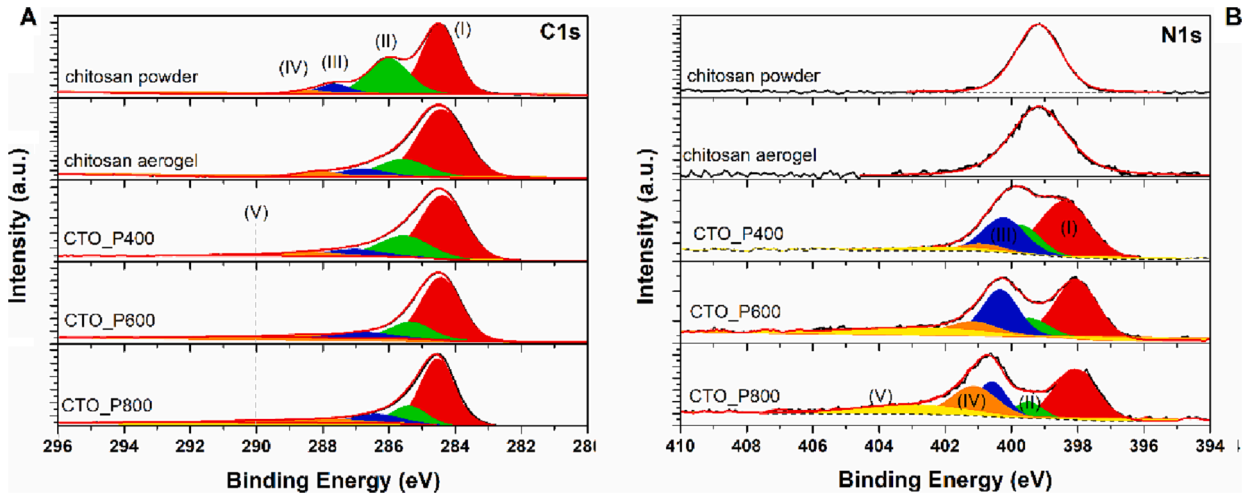

Fig. 2. (a) C1s HR spectra for all the samples analyzed, with chemical shift peaks positions highlighted by dashed grey vertical lines: peak (I) for C − C/H, peak (II) for C − O/N, peak (III) for O − C − O/C = O, peak (IV) for O − C = O/COOH and peak (V) for π − π* transition.; (b) N1s HR spectra for all the samples analyzed, with chemical shift peaks positions highlighted by dashed grey vertical lines: peak (I) for pyridinic-N, peak (II) for amino group, peak (III) for pyrrolic-N, peak (IV) for graphitic centers-N and peak (V) for graphitic valley-N or pyridine-N oxide bond.

biochars. Also, S. Dantas *et al.* [37] employed CO_2 adsorption to ascertain the pore size of micro-mesoporous carbons. The authors suggested a method to determine the PSD curves based on the reference theoretical isotherms, which employed Monte Carlo (MC) simulations in model pores of slit-shaped and cylindrical geometry. Similarly, P. I. Ravikovitch *et al.* [38] characterized various activated carbons using adsorption isotherms of different gases and models such as nonlocal density functional theory (NLDFT) and grand canonical Monte Carlo (GCMC). Multiple studies have shown that both NLDFT and GCMC methods can serve as a viable substitute for conventional phenomenological approaches, such as Dubinin-Radushkevich (DR), Horvath-Kawazoe (HK), and Barrett, Joyner, and Halenda (BJH) methods. Thus, we applied these methods in the CO_2 adsorption isotherms at 0 °C to determine the microporosity on chitosan-based biochar materials pyrolyzed at 400 and 600 °C (Figure S6, SM). A type I isotherm curve (IUPAC classification) [32] is observed for both samples. Interestingly, the S_{BET} increases from 400 to 600 °C, from 133 to 260 $m^2 \cdot g^{-1}$, while a shrinkage of the pores is observed, Table S2 and Figure S6. The increase of the pyrolysis temperature to 800 °C led to a very slow adsorption kinetic process for CO_2 at 0 °C (not shown), which may be related to the continuous shrinkage of the pores to smaller ultra-micropores making difficult the accessibility of CO_2 molecules into the pores. By examining the pore size distribution curves of the CTO_P600 sample, we can observe a significant number of pores with a size of approximately 0.35 nm. It is evident that if the pores continue to shrink as the pyrolysis temperature increases, CO_2 molecules may face difficulty entering these pores due to their dimensions, which are approximately 0.33 nm. This effect is particularly noticeable when utilizing the NLDFT and MC models.

Figure S7 shows the FESEM images of the different synthesized biochars. The sponge-like structure of the chitosan aerogel (Scheme S1) is retained after pyrolysis, even at higher temperatures (800 °C), and the open-hole structure can be observed at low magnification (500x). At higher magnification (50000x), the morphological characteristics of the pyrolyzed freeze-dried chitosan at different temperatures show a compact surface, almost without evidenced porosity, explaining the results obtained from the N_2-sorption isotherms. The inner regions of the particles seem to be dense, showing just some cracks, macro-, and meso-porosity. The latter case is more noticeable in the samples pyrolyzed at a higher temperature (*cf.* inset of Fig. S7c). The dense external surface of the chitosan-based biochar samples restricts N_2 diffusion to the interior only through narrow, unseen micropores at FESEM, which corresponds to a very slow process at 77 K (−196 °C) N_2 adsorption.

3.2. CO_2 adsorption-separation performance on biochar sorbents

3.2.1. Pure-component adsorption isotherms of CO_2, CH_4 and N_2

Pure CO_2, CH_4, and N_2 adsorption isotherms at 25 °C of the pyrolyzed chitosan-based samples are displayed in Fig. 3, while the determined Virial coefficients and Henry constants (K) for the adsorption are presented in Table 2. In all samples, CO_2 adsorption is significantly higher than the other two gases, which suggests that the materials have good potential for separating CO_2 from CH_4 and N_2. In more detail, increasing the pyrolysis temperature from 400 °C to 600 °C (samples CTO_P400 and CTO_P600) led to higher adsorption of the pure gases. The sample pyrolyzed at 800 °C had a slightly lower adsorption capacity for CO_2 than the sample pyrolyzed at 600 °C. The observed behavior can be attributed to the ongoing reduction in pore size resulting from the increase in pyrolysis temperature. This decrease in pore size could hinder the adsorption of CO_2 molecules within the pores.

Additionally, lower N content in the CTO_P800 sample, which, combined with a higher amount of graphitic center-N species (*cf.* Tables 1 and S1), can lead to a reduction in CO_2 adsorption when compared with the CTO_P600 adsorbent. Previous studies have shown that pyridone, pyridine, and pyrrole species enhanced CO_2 adsorption due to the Lewis acid-base and H-bonding interactions, which was corroborated by DFT [39] and XPS [28]. Despite the slightly reduced CO_2 adsorption for the CTO_P800 compared to the sample pyrolyzed at 600 °C, this sample still seems to be one of the most effective in this study for separating CO_2 from CH_4 and N_2, as the adsorbed amounts of CH_4 and N_2 are below the sensitivity of the method, while CTO_P600 shows the highest CH_4 and N_2 adsorption performance from the overall samples. The reason for the preferential adsorption of CO_2 over CH_4 and N_2 can be explained by the following factors: i) the molecular diameter of CO_2 (0.33 nm) is smaller than both CH_4 (0.38 nm) and N_2 (0.36 nm) molecules [28], making it easier for CO_2 to enter the ultra-micropores that are likely present in higher amount in the sample pyrolyzed at higher temperature [40,41]; ii) the adsorption process in these materials is primarily due to physisorption, which is an exothermic process. Hence, the higher the critical temperature of a gas, the easier it is to be adsorbed. The critical temperature of CO_2 (31.2 °C) is higher than of both CH_4 (−82.6 °C) and N_2 (−147 °C), thus CO_2 should be easier to adsorb [42-44]; iii) as stated above, CO_2 adsorption on biochar may be influenced by distinct interactions, including H-bonding, van der Waals attractions, and Lewis

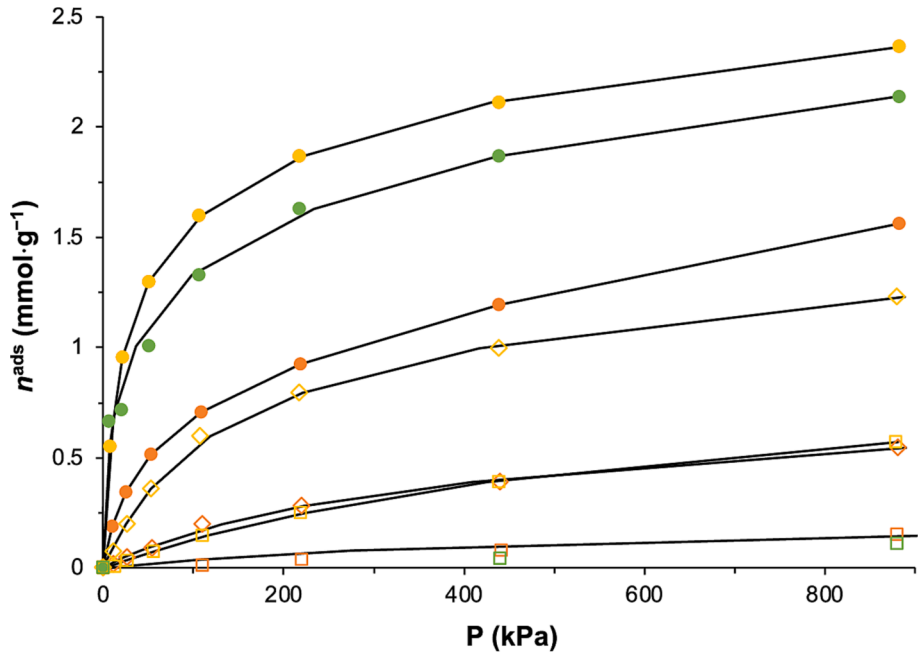

Fig. 3. Adsorption isotherms of pure CO_2 (circle symbols), CH_4 (diamond symbols), and N_2 (square symbols) gases at 25 °C in the pyrolyzed chitosan-based samples (orange – CTO_P400, yellow – CTO_P600, green – CTO_P800). The solid lines represent the fits of the Virial isotherm model to the experimental data. (For interpretation of the references to color in this figure legend, the reader is referred to the web version of this article.)

Table 2
Virial coefficients (C_1 and C_2) and Henry constants (K) for the adsorption of methane, carbon dioxide and nitrogen at 25 °C on the studied materials.

Gas	Sample	K (mol·kg^{-1}·kPa^{-1})	C_1 (kg·mol^{-1})	C_2 (kg·mol^{-1})^2	C_3 (kg·mol^{-1})^3 *	K^{CO2}/K^{CH4}	K^{CO2}/K^{N2}
CO_2	CTO_P400	3.45×10^{-2}	2.80	−0.57	–	14.94	69.70
	CTO_P600	1.47×10^{-1}	0.89	0.34	–	15.89	102.80
	CTO_P800	3.00×10^{-1}	2.47	−0.10	–	–	–
CH_4	CTO_P400	2.31×10^{-3}	1.92	0.93	–		
	CTO_P600	9.25×10^{-3}	0.51	0.84	–		
	CTO_P800	–	–	–	–		
N_2	CTO_P400	4.95×10^{-4}	7.22	1.00×10^{-15}	–		
	CTO_P600	1.43×10^{-3}	0.67	1.21	–		
	CTO_P800	–	–	–	–		

* The third virial coefficient (C_3) was neglected for all fitted adsorption isotherms.

acid-base interactions with N- and O- containing functional groups [45]. The CO_2 molecule has a higher quadrupolar moment than the CH_4 and N_2 molecules [46], thus being able to interact strongly with the functional groups of the biochar samples.

The pure gases adsorption isotherms at 35 °C for the pyrolyzed sample at 400 °C (Fig. S8a) show an expected behavior, *i.e.*, a slight decrease of the amount of gas adsorbed comparatively to the adsorption isotherms at 25 °C. However, the pyrolyzed samples at 600 and 800 °C (namely CTO_P600 (Fig. S8b) and CTO_P800 (not shown), respectively) show at 35 °C much lower adsorption capacities for all studied pure gases. The Henry constants and the Virial coefficients determined at 35 °C for each sample and gas studied are displayed in Table S3.

In general, all prepared pyrolyzed chitosan-based materials adsorb higher amounts of CO_2 than CH_4 and N_2 (Table 2). Considering the low N_2 adsorption capacity and Henry constants for N_2 for all the pyrolyzed materials, it is possible to generalize that these materials are weak N_2 adsorbents.

The mean selectivity for separation and equilibrium phase diagrams for the adsorbed phase can be calculated using a method proposed by Myers [47], with implementations described in previous works [48,49], using the Viral equation fitted to the adsorption data at 25 °C (Table 2) and the Ideal Adsorbed Solution Theory (IAST) [50]. Fig. 4 shows that the CTO_P600 has the highest selectivity values, presenting a three times

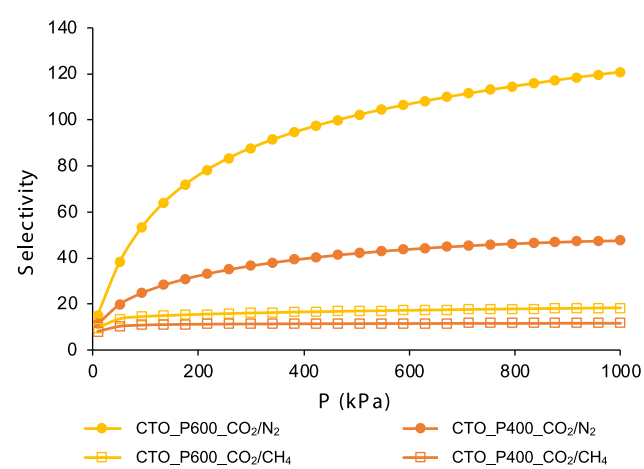

Fig. 4. Comparative mean selectivity, at 25 °C, of CTO_P400 (orange) and CTO_P600 (yellow), for the CO_2/CH_4 separation (square symbols) and for the CO_2/N_2 separation (circle symbols). (For interpretation of the references to color in this figure legend, the reader is referred to the web version of this article.)

higher selectivity value in the CO_2/N_2 separation, comparatively to CTO_P400. The high amounts of nitrogen species (between 6 and 10 wt. %) and the presence of ultramicroporosity (Figure S6) can contribute to the preferential adsorption of CO_2 over the CH_4 and N_2 [10]. No significant microporosity is observed with the low-temperature N_2 adsorption (less than 0.015 $cm^3 \cdot g^{-1}$). This suggests that the CO_2 uptake observed in the pyrolyzed samples may be adsorbed in very narrow micropores (ultramicropores) that are more selective for CO_2 [10], which were only detected by 0 °C CO_2 adsorption–desorption isotherms (Figure S6). Based on the PSD curves obtained using NLDFT and MC models (Fig. S6c-d), it can be observed that the CTO_P600 sample has a bimodal distribution of ultramicropores, with the peak centered at 0.35 and 0.50 nm. In contrast, the PSD curve of the CTO_P400 sample is wider and also shows the presence of micropores centered at 0.82 nm. The pores centered at 0.35 nm can physically separate CO_2 (0.33 nm) from CH_4 (0.38 nm) and N_2 (0.36 nm), and they exist in higher amounts in the CTO_P600 sample. However, other adsorption phenomena, for instance, chemical interactions, can be present in these samples as CTO_P400 and CTO_P600 samples have similar selectivity for CO_2/CH_4 separation (less than 20 at 500 kPa).

The evolution of the composition of the gas phase as a function of the composition of the adsorbed phase for two possible binary mixtures, CH_4/CO_2 and N_2/CO_2, are shown in Fig. 5. Each plot shows the variation in x (which is the molar fraction of the component gas in the adsorbed phase) with the variation in y (which is the molar fraction of the component gas in the gaseous phase at equilibrium conditions) at 500 kPa. For the binary mixture of CH_4 and CO_2 (Fig. 5a), at a molar fraction of about 0.5 (composition of a typical biogas feed) in the gas phase (yCH_4), the molar fraction of CH_4 in the adsorbed phase (xCH_4) is 0.080 on CTO_P400 and 0.061 on CTO_P600, at 500 kPa and 25 °C. This means that the adsorbed phase is richer in carbon dioxide than in methane for both materials. Moreover, CTO_P600 absorbs a higher amount of pure carbon dioxide (0.939 M composition) under these conditions. However, for the binary mixture of N_2 and CO_2 (Fig. 5b), at a molar fraction of N_2 of 0.8 (in the gas phase), the $x(N_2)$ on CTO_P400 and CTO_P600 are 0.02 and 0.03, respectively, which means that the adsorbed phase is almost pure carbon dioxide for both materials. The complete phase diagrams, presented in Figure S9, confirm the better performance of CTO_P600 material in terms of selectivity and adsorption capacity of CO_2.

The isosteric heats of adsorption for CO_2 were determined using the Clausius-Clapeyron equation, and the viral isotherms fitted to the CO_2 adsorption isotherms at 25 and 35 °C (Figure S10). According to the values estimated, CTO_P600 has the highest heat of adsorption for CO_2 among the tested sorbents. This implies that CTO_P600 has a stronger affinity for CO_2 molecules, resulting in a stronger dependence on the temperature, and the high value indicates that the adsorption of CO_2 is probably associated with a strong chemical interaction with the materials' surface that may be originated from a combination of narrow pores and the presence of N functional groups. Following CTO_P600, CTO_P800 exhibits a lower heat of adsorption, while CTO_P400 displays the lowest heat of adsorption for CO_2.

3.2.2. *Continuous flux N_2 and CO_2 adsorption-separation isotherms*

The CO_2 selectivity over N_2 under continuous flux conditions and atmospheric pressure was measured at 35 °C on the different biochars prepared in this study, and the weight increase is presented in Fig. 6a. All samples show a weight increase when the CO_2 gas (20 vol.%) is added to the system, exhibiting selectivity for CO_2 over N_2 even under gas mixture conditions.

The lowest CO_2 adsorption capacity over N_2 is found for the sample pyrolyzed at a lower temperature (CTO_P400), with a weight increase of only 0.42 $mmol \cdot g^{-1}$ (1.87 wt.%). The selectivity towards CO_2 under continuous flux conditions is enhanced by increasing the pyrolysis temperature, obtaining the highest adsorption for CO_2 over N_2 for the CTO_P800 samples (3.82 wt.% of weight increase, 0.87 $mmol \cdot g^{-1}$). This means that increasing the pyrolysis temperature to double allows the adsorption of twice the amount of CO_2 adsorbed in these conditions without significant differences in the weight loss of the sample during the pyrolysis process (section 2.2). Curiously, the increase in adsorption capacity/selectivity towards CO_2 is inversely proportional to the N content found on the samples (Tables 1 and S1, SM). This behavior can be related to the concomitant effect of higher amounts of ultramicropores (Table S2 and Figure S6), which usually appear at higher pyrolysis temperatures [40,41], allowing to physically separate these two gases more efficiently [43]. Also, the higher amount of graphitic valley-N or pyridine-N oxide species can play a relevant role as these species present favorable CO_2 adsorption [28,39]. The findings in Fig. 6b highlight the adsorption and desorption characteristics of different sorbents, specifically CTO_P800, CTO_P600, and CTO_P400, in the given experiment. Regarding the adsorption kinetics, CTO_P800 and CTO_P600 exhibit similar behavior by reaching approximately 70% of the total CO_2 adsorption within a 10 min period. This suggests that these sorbents have a rapid and efficient adsorption capacity. On the other hand, CTO_P400 displays a slower adsorption behavior, indicating a longer time is required to achieve the same level of CO_2 adsorption. During the desorption process, which was carried out under a pure N_2 flux at the same temperature as the adsorption measurement (35 °C), the results demonstrate the desorption efficiency of the sorbents. CTO_P800 exhibits the highest desorption efficiency, releasing 89% of the adsorbed CO_2 gas in less than 10 min. CTO_P600 follows closely with 79% desorption, while CTO_P400 shows a relatively lower desorption efficiency of 71%. These findings have promising implications for the

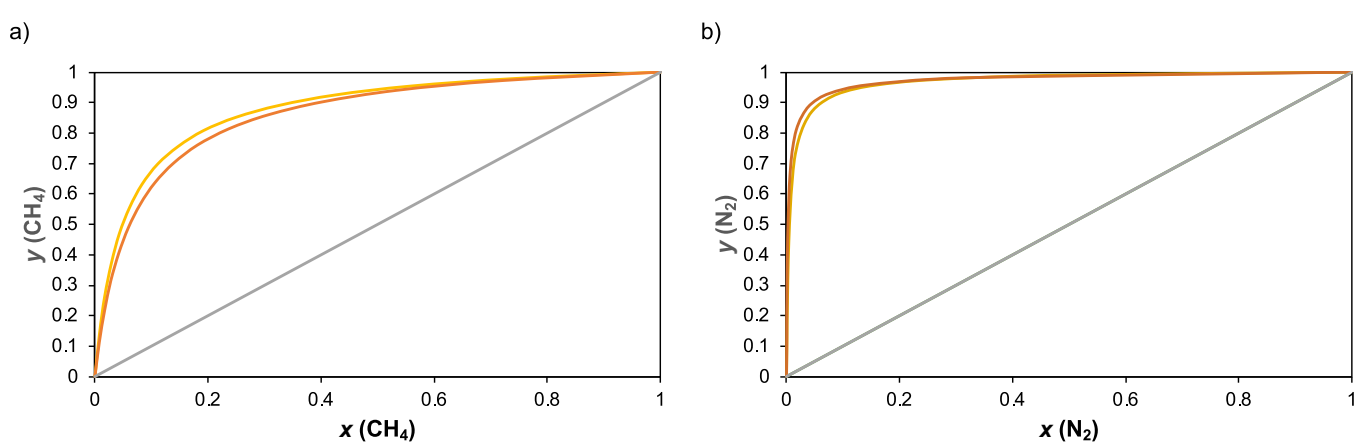

Fig. 5. Isothermal (at 25 °C), isobaric (at 500 kPa) xy diagrams of **a)** CO_2/CH_4 and **b)** CO_2/N_2 mixtures on the CTO_P400 (orange solid line) and CTO_P600 (yellow solid line) based materials. $y(CH_4)$, $x(CH_4)$, $y(N_2)$ and $x(N_2)$ are the molar fractions of methane and nitrogen in the gas and in the adsorbed phases, respectively. (For interpretation of the references to color in this figure legend, the reader is referred to the web version of this article.)

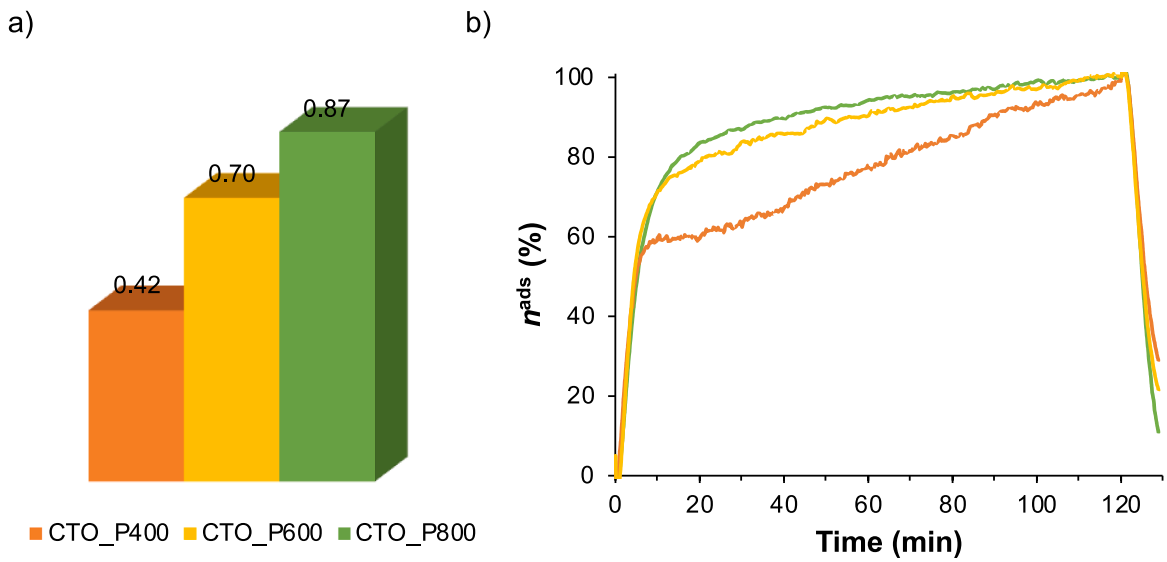

Fig. 6. a) total CO_2 adsorbed amounts (mmol·g^{-1}) at 35 °C and atmospheric pressure of a mixture of CO_2/N_2 gases (20 vol.% of CO_2) after 120 min of gas exposure and b) CO_2 adsorption kinetics under continuous flux of CO_2/N_2 gases at 35 °C and atmospheric pressure determined by TGA.

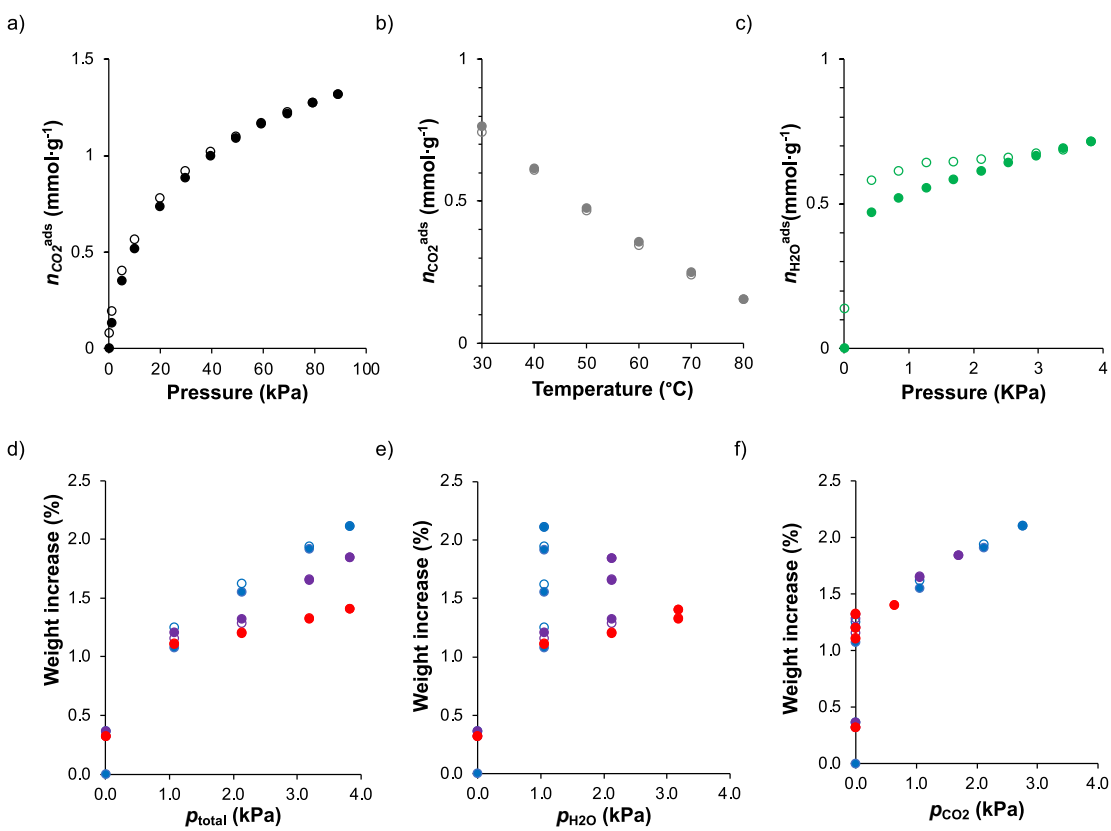

Fig. 7. Adsorption measurements on the CTO_P600 biochar: a) pure CO_2 adsorption isotherms (30 °C, up to 89 kPa, dm/dt = 0.001 %·min^{-1}); b) pure CO_2 adsorption isobar (20 kPa, up to 80 °C, dm/dt = 0.01 %·min^{-1}); c) H_2O vapor adsorption isotherms (30 °C, dm/dt = 0.001 %·min^{-1}; d) H_2O/CO_2 adsorption isotherm *vs* total pressure; e) H_2O/CO_2 adsorption isotherm *vs* water vapor partial pressure; and f) H_2O/CO_2 adsorption isotherm *vs* CO_2 partial pressure. Color scheme: 1st adsorption cycle – blue, 2nd cycle – purple, 3rd cycle – red. Filled symbols correspond to the adsorption processes, and empty symbols correspond to the desorption processes. (For interpretation of the references to color in this figure legend, the reader is referred to the web version of this article.)

potential use of CTO_P800 and CTO_P600 in cyclic adsorption–desorption measurements under industrial operating conditions. The efficient adsorption and high desorption efficiency make them suitable candidates for applications where repeated adsorption and regeneration cycles are required, such as in carbon capture and storage systems.

3.2.3. *CO_2 and water adsorption isotherms*

Pure CO_2 adsorption isotherms at 30 °C and up to 89 kPa and isobar at 20 kPa and up to 80 °C were performed on the CTO_P600 sample using a gravimetric apparatus, and the results are presented in Fig. 7. At the maximum pressure acquired in this measurement, CTO_P600 was able to adsorb 1.32 mmol·g^{-1} (~6 wt.%, Fig. 7a), which agrees with the

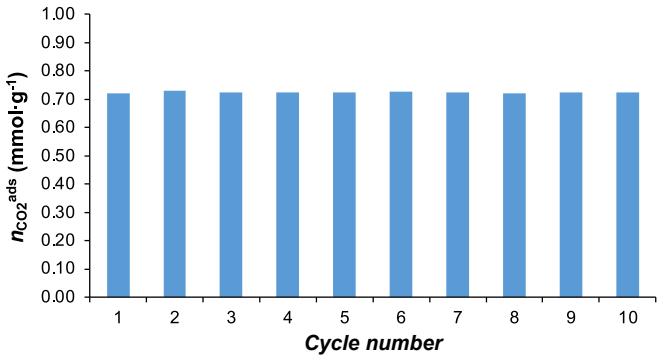

Fig. 8. Cyclic regenerability of the CTO_P600 biochar up to 10 consecutive adsorption (30 °C) – desorption (80 °C) cycles at 20 kPa using a dm/dt criterium of 0.01 %·min^{-1}.

values obtained in the previous section 3.2.1 by using the volumetric apparatus. After exposing the CTO_P600 sample to the CO_2 adsorption process at 30 °C and 89 kPa, it showed a decrease in the CO_2 amount adsorbed with the increase of the temperature (Fig. 7b) [51,52]. This means that physisorption is the dominant process in this sample [53]. The isobar equilibrium criterion (dm/dt) is 0.01 %·min^{-1}, 10 times lower than the equilibrium criterium used in the isotherm measurement, explaining the differences obtained in both methods regarding the CO_2 adsorption capacity at 30 °C. The reversibility of the process was evaluated by lowering the temperature, and the results showed that the same amount of desorbed CO_2 molecules were re-adsorbed by the CTO_P600 biochar.

Fig. 7c presents the H_2O vapor adsorption for the CTO_P600 sample, which can adsorb 0.66 mmol·g^{-1} (~1.2 wt.% of H_2O) at 4 kPa. This process takes 8.5 h to reach the maximum of adsorption, which is nearly 4 times lower than the water vapor uptake observed in our previous study for an amine-functionalized multiwalled carbon nanotube sample (CNT_SD_DETASi) [7]. An increase of the H_2O quantities adsorbed is observed when the H_2O vapor pressure increases, showing a type Ib isotherm (IUPAC classification) [32]. However, the desorption process, by reducing the humidity, is much slower than the adsorption process, resulting in hysteresis [54]. This behavior can be associated with the capillary condensation of the adsorbed water [55]. At the same operating conditions (pressure and temperature), this sample revealed a CO_2 adsorption capacity of 0.34 mmol·g^{-1} (~1.5 wt.%), which is half of the water vapor uptake and three times higher when compared with the adsorption capacity observed for the CNT_SD_DETASi sorbent [7]. Fig. 7 e-f depicts the adsorption behavior under H_2O/CO_2 mixtures, up to 3.8 kPa. CTO_P600 biochar displays a marked preference for CO_2 adsorption, especially at lower water vapor pressure, which is evident from the observed increase in weight after addition of CO_2 gas. As the H_2O pressure is increased from 1.06 kPa to 3.8 kPa, the amount of CO_2 adsorbed decreases from 1.03 wt.% to 0.08 wt.%, respectively. Thus, considering our previous work, CTO_P600 sorbent appears to be more interesting from the economic and sustainable material preparation point of view, but also regarding the performance in the CO_2 adsorption separation process even when moisture is present.

3.2.4. Adsorbent regeneration capacity

The regeneration ability of adsorbents is a relevant characteristic for understanding how they will behave under long-time operation processes. Thus, a fast-cycle adsorption/desorption study of 10 cycles on the CTO_P600 sample was performed after the adsorption isotherm (Fig. 8). The adsorption process was carried out at ~ 20 kPa (0.2 bar) and 30 °C while the desorption process was done at 80 °C under vacuum. The obtained data indicate that CTO_P600 biochar performs well under cyclic adsorption–desorption processes retaining the same CO_2 adsorption capacity after each cycle.

3.3. Comparison with other materials

The capacities for CO_2, N_2, and CH_4 adsorption of the best-performing biochar (CTO_P600) for the CO_2/N_2 and CO_2/CH_4 separation are compared with other carbonaceous sorbents in Table 3.

All biochar and activated carbon compiled in this Table can adsorb CO_2 in the temperature range of 0 – 35 °C, with the highest CO_2 uptake values observed for the activated carbon materials (AC-KOH-D-5–700 [33], Cell-UK [56], and BC800K [57]) typically obtained by a second-step of thermal activation (at temperatures of 700 or 800 °C) under the presence of high amounts of KOH. Despite these materials having high CO_2 adsorption capacity (between 2.3 and 4.4 mmol·g^{-1}) at 20 – 25 °C and 100 kPa and seemingly showing high CO_2 selectivity over N_2, both CH_4 and N_2 adsorption capacities were not measured or provided on most of the cases, as well as CO_2 selectivity over CH_4. Moreover, in the only activated carbon, where the N_2 adsorption capacity is provided (Cell-UK), the obtained value is much higher than the one obtained for the biochar studied in this work. Additionally, all these carbonaceous sorbents are not sustainable from a preparation standpoint, as they require high amounts of KOH for activation and are obtained in powder form, which requires further processing for industrial use, *e.g.*, pelletization, to avoid pressure drop issues. Some biochars reported in the literature (BC-CO_2-0.1–800 [33] and C–Char_800 [58]) seem to be promising for CO_2 uptake, showing high CO_2 adsorption capacities (2.2 and 4.0 mmol·g^{-1}, respectively) and selectivity over N_2 (55) in the case of the BC–CO_2-0.1–800 sorbent [33]. However, the preparation of these biochar sorbents is made under a CO_2 atmosphere, and in the latter case, activation is necessary. These materials are also prepared in powdered form.

All biochar sorbents prepared in this study perform better than CNT_COOH_DETASi sorbent [7], which had the highest CO_2 adsorption capacity and selectivity towards CO_2 among multi-walled carbon nanotubes in our previous study. Additionally, CTO_P600 showed lower water vapor uptake when compared with the CNT_SD_DETASi sorbent [7] (not compared in Table 3, *cf.* reference [7]), thus being a highly promising CO_2 adsorbent even under moisture conditions. CTO_P600 biochar and Chit_supCO_2_P800 sorbent [10] showed similar CO_2 uptake and CO_2/CH_4 selectivity under the same operating conditions. Both sorbents have the potential for industrial application due to their shape. However, Chit_supCO_2_P800 has a much more complex synthesis procedure involving chitosan beads production, followed by a solvent-switch method (from water to ethanol) and supercritical CO_2 drying technology (which is more expensive to perform than freeze-drying), and a higher pyrolysis temperature.

4. Conclusions

A sponge-like chitosan freeze-dried aerogel was successfully pyrolyzed at different temperatures to create sponge-like biochars with varying textural properties. XPS data revealed that the amino groups in the sponge-like chitosan aerogel underwent degradation and transformations during the pyrolysis process, resulting in various types and levels of N-species, such as pyridinic-N, pyrrolic-N or pyridone, graphitic center-N and graphitic valley-N or pyridine-N oxide species. The resulting biochars were tested for their ability to adsorb CO_2, CH_4, and N_2 at different temperatures and pressures. In general, the increase in pyrolysis temperature enhanced the CO_2 adsorption capacity and selectivity for CO_2/CH_4 and CO_2/N_2 separation. CO_2 isobar measurements up to 80 °C showed that physisorption was the dominant adsorption process in CTO_P600 sorbent. The CTO_P600 biochar showed tolerance to moisture and retained its CO_2 adsorption capacity after being reused for 10 cycles in pure CO_2 adsorption-desorption conditions, suggesting potential for surface regeneration and application in cyclic separation processes at the industrial level. The sustainable production of these biochars without requiring extra activation or functionalization procedures, coupled with their sponge-like aerogel shape, renders them

Table 3
Capacities of different carbonaceous sorbents in the CO_2 adsorption-separation.

Materials[REF]	N content ($mmol \cdot g^{-1}$)	CO_2 uptake ($mmol \cdot g^{-1}$)	CH_4 uptake ($mmol \cdot g^{-1}$)	N_2 uptake ($mmol \cdot g^{-1}$)	T_{ads}[a] (°C)	P^b_{ads} (kPa)	Selectivity[c]	
							CO_2/CH_4	CO_2/N_2
BC-CO_2-0.1-800[33][d]	–	3.5	–	–	0	100	–	–
AC-KOH-D-5-700[33][e]	–	6.1	–	–			–	–
BC-CO_2-0.1-800[33][d]	–	~4.0	–	–	25	100	–	55
AC-KOH-D-5-700[33][e]	–	~2.3	–	–			–	57
C-Char_800[58][f]	–	2.2	–	–	20	100	–	–
Cell-UK[56][g]	2.29 [h]	4.4	–	0.42	25	100	–	70
BC800K[57][i]	0.15[j]	3.2	–	–		100	28	125
Chit_supCO_2_P800	12.94[j]	~1.3	0.02	–	25	100	40	–
[10]		~2.5	0.15	–		1000	130	–
CNT_COOH_DETASi	6.10 [h]	0.48	–	–	30	89	–	–
[7]		–	–	–	35	100	–	0.33 $mmol \cdot g^{-1}$[l]
This study								
CTO_P400	8.9 [h] (9.9)[j]	~0.75	~0.2	~0.05	25	100	~25	~10
		~1.6	~0.5	~0.02		~900	~39	~10
		~0.55	–	–	35	100	–	0.42 $mmol \cdot g^{-1}$[l]
CTO_P600	6.5 [h] (8.9)[j]	~1.6	~0.6	~0.2	25	100	~55	~12
		~2.4	~1.2	~0.5		~900	~120	~13
		~1.3	–	–	30	89	–	–
		~0.65	–	–	35	100	–	0.70 $mmol \cdot g^{-1}$[l]
CTO_P800	5.1 [h] (6.4)[j]	~1.3	–	~0.05	25	100	–	n.d.[m]
		~2.2	–	~0.15		~900	–	n.d.[m]
		~0.9	–	–	35	100	–	0.87 $mmol \cdot g^{-1}$[l]

[a] Adsorption temperature; [b]Adsorption pressure; [c]Determined by applying the IAST model on the pure adsorption isotherms –CO_2/CH_4:50/50 and CO2/N2:50/50; [d]Biochar derived from vine shoots produced by single-step oxidation, pyrolysed under CO_2 flux, under 0.1 MPa pressure at 800 °C; [e]AC denotes for activated carbon obtained through a physically mixture of the biochar with KOH in an agate mortar at KOH/biochar mass ratio of 5:1 and pyrolysis temperature of 700 °C; [f]fast pyrolyzed biochar derived from cotton stalk and post-treated with CO_2 at 800 °C: [g]Cell-UK denotes for heteroatoms doped cellulose-based porous activated carbon, where U represents UREA as N doping agent and K denotes for KOH activating agent; The sample was prepared at 800 °C; [h]determined from XPS; [i]activated carbon derived from pine wood using a two-step procedure: pyrolysis at 300 °C under N_2 flux followed by wet impregnation with KOH (4 h, and drying at 105 °C for 48 h) and thermal treatment at 800 °C (4 h); [j]determined from elemental analysis; [l]CO_2 weight increase - adsorption conditions: 20% CO_2 in a N_2/CO_2 binary gas mixture under continuous flux conditions; [m]n.d. denotes for non-determined.

highly desirable for CO_2 adsorption-separation processes applicable in industrial settings.

Author contributions

The manuscript was written through the contributions of all authors. All authors approved to the final version of the manuscript.

Declaration of Competing Interest

The authors declare that they have no known competing financial interests or personal relationships that could have appeared to influence the work reported in this paper.

Data availability

Data will be made available on request.

Acknowledgments

This work was developed within the scope of the projects UIDB/50011/2020, UIDP/50011/2020 and LA/P/0006/2020 (CICECO), and UIDB/04028/2020 and UIDP/04028/2020 (CERENA), financed by Portuguese national funds through *Fundação para a Ciência e a Tecnologia* (FCT)/MEC (PIDDAC), and when applicable co-financed by the European Regional Development Fund (ERDF) under the PT2020 partnership agreement. M.A.O.L thanks IIT for the research support, FCT for the Junior Researcher Position (2021.01158.CEECIND), and the funding from the European Union's Horizon Europe research and innovation program under the Marie Skłodowska-Curie PF grant agreement No 101090287. M.B. acknowledges FCT for the Ph.D. Grant (SFRH/BD/147239/2019).

Appendix A. Supplementary data

Supplementary data to this article can be found online at https://doi.org/10.1016/j.cej.2023.144005.

References

[1] X. Wang, C. Song, Carbon capture from flue gas and the atmosphere: A perspective, Front. Energy Res. 8 (2020), https://doi.org/10.3389/fenrg.2020.560849.
[2] X. He, A review of material development in the field of carbon capture and the application of membrane-based processes in power plants and energy-intensive industries, Energy Sustain. Soc. 8 (2018), https://doi.org/10.1186/s13705-018-0177-9.
[3] S. Chaemchuen, N.A. Kabir, K. Zhou, F. Verpoort, Metal-organic frameworks for upgrading biogas via CO_2 adsorption to biogas green energy, Chem. Soc. Rev. 42 (2013) 9304–9332, https://doi.org/10.1039/c3cs60244c.
[4] I. Ghiat, T. Al-Ansari, A review of carbon capture and utilisation as a CO_2 abatement opportunity within the EWF nexus, J. CO_2 Util. 45 (2021), 101432, https://doi.org/10.1016/j.jcou.2020.101432.
[5] A.I. Osman, M. Hefny, M.I.A. Abdel Maksoud, A.M. Elgarahy, D.W. Rooney, Recent advances in carbon capture storage and utilisation technologies: a review, Environ. Chem. Lett. 19 (2021) 797–849, https://doi.org/10.1007/s10311-020-01133-3.
[6] O.W. Awe, Y. Zhao, A. Nzihou, D.P. Minh, N. Lyczko, A Review of Biogas Utilisation, Purification and Upgrading Technologies, Waste Biomass Valorization. 8 (2018) 267–283, https://doi.org/10.1007/s12649-016-9826-4.
[7] M.A.O. Lourenço, M. Fontana, P. Jagdale, C.F. Pirri, S. Bocchini, Improved CO_2 adsorption properties through amine functionalization of multi-walled carbon nanotubes, Chem. Eng. J. 414 (2021), 128763, https://doi.org/10.1016/j.cej.2021.128763.
[8] H. Zhang, Z. Yu, Q. Huang, A Review: Utilization of Biochar for Wastewater Treatment, in: A. Bhatnagar (Ed.), Application of Adsorbents for Water Pollution Control, Bentham eBooks, 2012, pp. 413–431, https://doi.org/10.2174/9781608052691120101041 3.

[9] Y. Qiao, C. Wu, Nitrogen enriched biochar used as CO_2 adsorbents: a brief review, Carbon Capture Science & Technology. 2 (2022), 100018, https://doi.org/10.1016/j.ccst.2021.100018.

[10] M.A.O. Lourenço, C. Nunes, J.R.B. Gomes, J. Pires, M.L. Pinto, P. Ferreira, Pyrolyzed chitosan-based materials for CO_2/CH_4 separation, Chem. Eng. J. 362 (2019) 364–374, https://doi.org/10.1016/j.cej.2018.12.180.

[11] S. Sethupathi, M. Zhang, A. Rajapaksha, S. Lee, N. Mohamad Nor, A. Mohamed, M. Al-Wabel, S. Lee, Y. Ok, Biochars as potential adsorbers of CH_4, CO_2 and H_2S, Sustainability. 9 (2017) 121.

[12] R. Afonso, M. Sardo, L. Mafra, J.R.B. Gomes, Unravelling the structure of chemisorbed CO_2 species in mesoporous aminosilicas: A critical survey, Environ. Sci. Tech. 53 (2019) 2758–2767, https://doi.org/10.1021/acs.est.8b05978.

[13] L. Mafra, T. Čendak, S. Schneider, P.V. Wiper, J. Pires, J.R.B. Gomes, M.L. Pinto, Structure of chemisorbed CO_2 species in amine-functionalized mesoporous silicas studied by solid-state NMR and computer modeling, J. Am. Chem. Soc. 139 (2017) 389–408, https://doi.org/10.1021/jacs.6b11081.

[14] L. Mafra, T. Čendak, S. Schneider, P.V. Wiper, J. Pires, J.R.B. Gomes, M.L. Pinto, Amine functionalized porous silica for CO_2/CH_4 separation by adsorption: Which amine and why, Chem. Eng. J. 336 (2018) 612–621, https://doi.org/10.1016/j.cej.2017.12.061.

[15] M.L. Pinto, L. Mafra, J.M. Guil, J. Pires, J. Rocha, Adsorption and activation of CO_2 by amine-modified nanoporous materials studied by solid-state NMR and $^{13}CO_2$ adsorption, Chem. Mater. 23 (2011) 1387–1395, https://doi.org/10.1021/cm1029563.

[16] M. Sardo, R. Afonso, J. Juźków, M. Pacheco, M. Bordonhos, M.L. Pinto, J.R. B. Gomes, L. Mafra, Unravelling moisture-induced CO_2 chemisorption mechanisms in amine-modified sorbents at the molecular scale, J Mater Chem A Mater. 9 (2021) 5542–5555, https://doi.org/10.1039/D0TA09808F.

[17] J. Wang, P. Zhang, L. Liu, Y. Zhang, J. Yang, Z. Zeng, S. Deng, Controllable synthesis of bifunctional porous carbon for efficient gas-mixture separation and high-performance supercapacitor, Chem. Eng. J. 348 (2018) 57–66, https://doi.org/10.1016/j.cej.2018.04.188.

[18] I. Durán, N. Álvarez-Gutiérrez, F. Rubiera, C. Pevida, Biogas purification by means of adsorption on pine sawdust-based activated carbon: Impact of water vapor, Chem. Eng. J. 353 (2018) 197–207, https://doi.org/10.1016/j.cej.2018.07.100.

[19] M.A.O. Lourenco, J. Zeng, P. Jagdale, M. Castellino, A. Sacco, M.A. Farkhondehfal, C.F. Pirri, Biochar/Zinc Oxide Composites as Effective Catalysts for Electrochemical CO_2 Reduction, ACS Sustain. Chem. Eng. 9 (2021) 5445–5453, https://doi.org/10.1021/acssuschemeng.1c00837.

[20] I. Corazzari, R. Nisticò, F. Turci, M.G. Faga, F. Franzoso, S. Tabasso, G. Magnacca, Advanced physico-chemical characterization of chitosan by means of TGA coupled on-line with FTIR and GCMS: Thermal degradation and water adsorption capacity, Polym. Degrad. Stab. 112 (2015) 1–9, https://doi.org/10.1016/j.polymdegradstab.2014.12.006.

[21] M.K. Jang, B.G. Kong, Y. Il Jeong, C.H. Lee, J.W. Nah, Physicochemical characterization of α-chitin, β-chitin, and γ-chitin separated from natural resources, J. Polym. Sci. A Polym. Chem. 42 (2004) 3423–3432, https://doi.org/10.1002/pola.20176.

[22] P. Avetta, R. Nisticò, M.G. Faga, D. D'Angelo, E.A. Boot, R. Lamberti, S. Martorana, P. Calza, D. Fabbri, G. Magnacca, Hernia-repair prosthetic devices functionalised with chitosan and ciprofloxacin coating: Controlled release and antibacterial activity, J. Mater. Chem. B 2 (2014) 5287–5294, https://doi.org/10.1039/c4tb00236a.

[23] J.B. Marroquin, K.Y. Rhee, S.J. Park, Chitosan nanocomposite films: Enhanced electrical conductivity, thermal stability, and mechanical properties, Carbohydr. Polym. 92 (2013) 1783–1791, https://doi.org/10.1016/j.carbpol.2012.11.042.

[24] B. Jurado-López, R.S. Vieira, R.B. Rabelo, M.M. Beppu, J. Casado, E. Rodríguez-Castellón, Formation of complexes between functionalized chitosan membranes and copper: A study by angle resolved XPS, Mater. Chem. Phys. 185 (2017) 152–161, https://doi.org/10.1016/j.matchemphys.2016.10.018.

[25] P.C. Li, G.M. Liao, S.R. Kumar, C.M. Shih, C.C. Yang, D.M. Wang, S.J. Lue, Fabrication and characterization of chitosan nanoparticle-incorporated quaternized poly(vinylalcohol) composite membranes as solid electrolytes for direct methanol alkaline fuel cells, Electrochim Acta. 187 (2016) 616–628, https://doi.org/10.1016/j.electacta.2015.11.117.

[26] Y.X. Seow, Y.H. Tan, N.M. Mubarak, J. Kansedo, M. Khalid, M.L. Ibrahim, M. Ghasemi, A review on biochar production from different biomass wastes by recent carbonization technologies and its sustainable applications, J. Environ. Chem. Eng. 10 (2022), 107017, https://doi.org/10.1016/j.jece.2021.107017.

[27] L. Klüpfel, M. Keiluweit, M. Kleber, M. Sander, Redox properties of plant biomass-derived black carbon (biochar), Environ. Sci. Tech. 48 (2014) 5601–5611, https://doi.org/10.1021/es500906d.

[28] X. Fan, L. Zhang, G. Zhang, Z. Shu, J. Shi, Chitosan derived nitrogen-doped microporous carbons for high performance CO_2 capture, Carbon 61 (2013) 423–430, https://doi.org/10.1016/j.carbon.2013.05.026.

[29] A. Olejniczak, M. Lezanska, J. Wloch, A. Kucinska, J.P. Lukaszewicz, Novel nitrogen-containing mesoporous carbons prepared from chitosan, J. Mater. Chem. A 1 (2013) 8961, https://doi.org/10.1039/c3ta11337j.

[30] R. Arrigo, M. Hävecker, R. Schlögl, D.S. Su, Dynamic surface rearrangement and thermal stability of nitrogen functional groups on carbon nanotubes, Chem. Commun. (2008) 4891–4893, https://doi.org/10.1039/b812769g.

[31] M.A. Wójtowicz, J.R. Pels, J.A. Moulijn, The fate of nitrogen functionalities in coal during pyrolysis and combustion, Fuel 74 (1995) 507–516, https://doi.org/10.1016/0016-2361(95)98352-F.

[32] M. Thommes, K. Kaneko, A.V. Neimark, J.P. Olivier, F. Rodriguez-Reinoso, J. Rouquerol, K.S.W. Sing, Physisorption of gases, with special reference to the evaluation of surface area and pore size distribution (IUPAC Technical Report), Pure and Applied, Chemistry 87 (2015) 1051–1069, https://doi.org/10.1515/pac-2014-1117.

[33] J.J. Manyà, B. González, M. Azuara, G. Arner, Ultra-microporous adsorbents prepared from vine shoots-derived biochar with high CO_2 uptake and CO_2/N_2 selectivity, Chem. Eng. J. 345 (2018) 631–639, https://doi.org/10.1016/j.cej.2018.01.092.

[34] K.C. Kim, T.U. Yoon, Y.S. Bae, Applicability of using CO_2 adsorption isotherms to determine BET surface areas of microporous materials, Microporous Mesoporous Mater. 224 (2016) 294–301, https://doi.org/10.1016/j.micromeso.2016.01.003.

[35] P. Maziarka, C. Wurzer, P.J. Arauzo, A. Dieguez-Alonso, O. Mašek, F. Ronsse, Do you BET on routine? The reliability of N_2 physisorption for the quantitative assessment of biochar's surface area, Chem. Eng. J. 418 (2021), 129234, https://doi.org/10.1016/j.cej.2021.129234.

[36] A. Dieguez-Alonso, A. Anca-Couce, V. Frišták, E. Moreno-Jiménez, M. Bacher, T. D. Bucheli, G. Cimò, P. Conte, N. Hagemann, A. Haller, I. Hilber, O. Husson, C. I. Kammann, N. Kienzl, J. Leifeld, T. Rosenau, G. Soja, H.P. Schmidt, Designing biochar properties through the blending of biomass feedstock with metals: Impact on oxyanions adsorption behavior, Chemosphere 214 (2019) 743–753, https://doi.org/10.1016/j.chemosphere.2018.09.091.

[37] S. Dantas, K.C. Struckhoff, M. Thommes, A.V. Neimark, Pore size characterization of micro-mesoporous carbons using CO_2 adsorption, Carbon 173 (2021) 842–848, https://doi.org/10.1016/j.carbon.2020.11.059.

[38] P.I. Ravikovitch, A. Vishnyakov, R. Russo, A.V. Neimark, Unified approach to pore size characterization of microporous carbonaceous materials from N_2, Ar, and CO_2 adsorption isotherms, Langmuir 16 (2000) 2311–2320, https://doi.org/10.1021/la991011c.

[39] G. Lim, K.B. Lee, H.C. Ham, Effect of N-Containing Functional Groups on CO_2 Adsorption of Carbonaceous Materials: A Density Functional Theory Approach, J. Phys. Chem. C 120 (2016) 8087–8095, https://doi.org/10.1021/acs.jpcc.5b12090.

[40] R. Chatterjee, B. Sajjadi, W.Y. Chen, D.L. Mattern, N. Hammer, V. Raman, A. Dorris, Effect of pyrolysis temperature on physicochemical properties and acoustic-based amination of biochar for efficient CO_2 adsorption, Front. Energy Res. 8 (2020) 1–18, https://doi.org/10.3389/fenrg.2020.00085.

[41] S. Liu, S. Peng, B. Zhang, B. Xue, Z. Yang, S. Wang, G. Xu, Effects of biochar pyrolysis temperature on thermal properties of polyethylene glycol/biochar composites as shape-stable biocomposite phase change materials, RSC Adv. 12 (2022) 9587–9598, https://doi.org/10.1039/d1ra09167k.

[42] M. Sadeghi, M.A. Semsarzadeh, M. Barikani, B. Ghalei, The effect of urethane and urea content on the gas permeation properties of poly(urethane-urea) membranes, J Memb Sci. 354 (2010) 40–47, https://doi.org/10.1016/j.memsci.2010.02.070.

[43] M.M. Talakesh, M. Sadeghi, M.P. Chenar, A. Khosravi, Gas separation properties of poly(ethylene glycol)/poly(tetramethylene glycol) based polyurethane membranes, J. Memb. Sci. 415–416 (2012) 469–477, https://doi.org/10.1016/j.memsci.2012.05.033.

[44] D. Feng, D. Guo, Y. Zhang, S. Sun, Y. Zhao, G. Chang, Q. Guo, Y. Qin, Adsorption-enrichment characterization of CO_2 and dynamic retention of free NH_3 in functionalized biochar with $H_2O/NH_3{\cdot}H_2O$ activation for promotion of new ammonia-based carbon capture, Chem. Eng. J. 409 (2021), 128193, https://doi.org/10.1016/j.cej.2020.128193.

[45] A.N. Shafawi, A.R. Mohamed, P. Lahijani, M. Mohammadi, Recent advances in developing engineered biochar for CO_2 capture: An insight into the biochar modification approaches, J. Environ. Chem. Eng. 9 (6) (2021), 106869, https://doi.org/10.1016/j.jece.2021.106869.

[46] G. Aguilar-Armenta, M.E. Patino-Iglesias, R. Leyva-Ramos, Adsorption kinetic behaviour of pure CO_2, N_2 and CH_4 in natural clinoptilolite at different temperatures, Adsorpt. Sci. Technol. 21 (2003) 81–92, https://doi.org/10.1260/026361703603699831.

[47] A.L. Myers, Equation of State for Adsorption of Gases and Their Mixtures in Porous Materials, Adsorption 9 (2003) 9–16, https://doi.org/10.1023/A:1023807128914.

[48] M.L. Pinto, J. Pires, J. Rocha, Porous Materials Prepared from Clays for the Upgrade of Landfill Gas, J. Phys. Chem. C 112 (2008) 14394–14402, https://doi.org/10.1021/jp803015d.

[49] J. Pires, V.K. Saini, M.L. Pinto, Studies on selective adsorption of biogas components on pillared clays: Approach for biogas improvement, Environ. Sci. Tech. 42 (2008) 8727–8732, https://doi.org/10.1021/es8014666.

[50] A.L. Myers, J.M. Prausnitz, Thermodynamics of mixed-gas adsorption, AIChE J. 11 (1965) 121–127, https://doi.org/10.1002/aic.690110125.

[51] F. Su, C. Lu, W. Cnen, H. Bai, J.F. Hwang, Capture of CO_2 from flue gas via multiwalled carbon nanotubes, Sci. Total Environ. 407 (2009) 3017–3023, https://doi.org/10.1016/j.scitotenv.2009.01.007.

[52] B. Yang, H. Hu, X. Zhang, Z. Li, L. Lei, Pretreated multi-walled carbon nanotube adsorbents with amine-grafting for CO_2 removal in confined space, RSC Adv. 4 (2014) 56224–56234, https://doi.org/10.1039/C4RA11271G.

[53] Q. Ye, J. Jiang, C. Wang, Y. Liu, H. Pan, Y. Shi, Adsorption of low-concentration carbon dioxide on amine-modified carbon nanotubes at ambient temperature, Energy Fuel 26 (2012) 2497–2504, https://doi.org/10.1021/ef201699w.

[54] C. Wang, Y. Xing, Y. Lei, Y. Xia, C. Zhang, R. Zhang, S. Wang, P. Chen, S. Zhu, J. Li, X. Gui, Adsorption of water on carbon materials: The formation of "water bridge" and its effect on water adsorption, Colloids Surf. A Physicochem. Eng. Asp. 631 (2021), 127719, https://doi.org/10.1016/j.colsurfa.2021.127719.

[55] F.V.S. Lopes, C.A. Grande, A.M. Ribeiro, J.M. Loureiro, O. Evaggelos, V. Nikolakis, A.E. Rodrigues, Adsorption of H_2, CO_2, CH_4, CO, N_2 and H_2O in activated carbon and zeolite for hydrogen production, Sep. Sci. Technol. 44 (2009) 1045–1073, https://doi.org/10.1080/01496390902729130.

[56] A. Rehman, G. Nazir, K. Yop Rhee, S.J. Park, A rational design of cellulose-based heteroatom-doped porous carbons: Promising contenders for CO_2 adsorption and separation, Chem. Eng. J. 420 (2021), 130421, https://doi.org/10.1016/j.cej.2021.130421.

[57] K. Li, D. Zhang, X. Niu, H. Guo, Y. Yu, Z. Tang, Z. Lin, M. Fu, Insights into CO_2 adsorption on KOH-activated biochars derived from the mixed sewage sludge and pine sawdust, Sci. Total Environ. 826 (2022), 154133, https://doi.org/10.1016/j.scitotenv.2022.154133.

[58] X. Zhang, S. Zhang, H. Yang, Y. Feng, Y. Chen, X. Wang, H. Chen, Nitrogen enriched biochar modified by high temperature CO_2-ammonia treatment: Characterization and adsorption of CO_2, Chem. Eng. J. 257 (2014) 20–27, https://doi.org/10.1016/j.cej.2014.07.024.